

See discussions, stats, and author profiles for this publication at:  
<https://www.researchgate.net/publication/223256699>

# Nonadiabatic wave packet dynamics on the coupled X<sup>2</sup>A<sub>1</sub>/A<sup>2</sup>B<sub>2</sub> electronic states of NO<sub>2</sub> based on new ab initio potential energy surfaces

ARTICLE *in* CHEMICAL PHYSICS · SEPTEMBER 2000

Impact Factor: 1.65 · DOI: 10.1016/S0301-0104(00)00204-4

CITATIONS

53

READS

17

5 AUTHORS, INCLUDING:



**Susanta Mahapatra**

University of Hyderabad

114 PUBLICATIONS 1,636 CITATIONS

SEE PROFILE



**Horst Köppel**

Universität Heidelberg

240 PUBLICATIONS 5,952 CITATIONS

SEE PROFILE



**Wolfgang Wenzel**

Karlsruhe Institute of Technology

312 PUBLICATIONS 3,705 CITATIONS

SEE PROFILE

# Nonadiabatic wave packet dynamics on the coupled $\tilde{X}^2A_1/\tilde{A}^2B_2$ electronic states of $NO_2$ based on new ab initio potential energy surfaces

S. Mahapatra<sup>a</sup>, H. Köppel<sup>a,\*</sup>, L.S. Cederbaum<sup>a</sup>, P. Stampfuß<sup>b</sup>, W. Wenzel<sup>b</sup>

<sup>a</sup> Department of Theoretical Chemistry, University of Heidelberg, Im Neuenheimer Feld 229, D-69120 Heidelberg, Germany

<sup>b</sup> Department of Theoretical Physics I, University of Dortmund, D-44221 Dortmund, Germany

Received 6 April 2000; in final form 5 June 2000

## Abstract

We report new accurate ab initio potential energy surfaces (PESs) for the ground ( $\tilde{X}^2A_1$ ) and first excited ( $\tilde{A}^2B_2$ ) electronic states of  $NO_2$ . The adiabatic potential energy data are calculated by the configuration-selecting multi-reference configuration-interaction method employing the cc-pVTZ basis set. We diabatize the adiabatic potential energy data and investigate the nuclear dynamics on these coupled electronic states by a time-dependent wave packet method. First, we investigate the photodetachment spectrum of  $NO_2^-$  for a transition to the  $\tilde{A}^2B_2$  state and compare our findings with the available experimental results. The agreement is very satisfactory. In addition, we examine the femtosecond decay of the  $\tilde{A}^2B_2$  diabatic electronic population revealing the impact of the nonadiabatic coupling on the time-dependent dynamics (internal conversion process) of  $NO_2$ . The present study based on more accurate ab initio PESs enables us to confirm our earlier estimate of the vibronic coupling strength near the energetic minimum of the  $\tilde{X}^2A_1$ – $\tilde{A}^2B_2$  crossing seam. © 2000 Elsevier Science B.V. All rights reserved.

## 1. Introduction

Vibronic interactions between different electronic potential energy surfaces (PESs) are a generic feature of polyatomic molecules. Such interactions become strong for near-degenerate or degenerate electronic states, and the spectroscopy and dynamics of a molecule are strongly influenced by the associated nonadiabatic couplings [1–4]. A typical scenario in polyatomic systems is the

occurrence of *conical intersections* of PESs, where the dominating coupling term is of first order in the nuclear coordinates [1–12]. Their importance is documented by the appearance of many scientific articles in the present special issue. For additional, mostly quite early work on the quantum dynamics of conically intersecting surfaces see, for example, Refs. [1–4] and references therein. In dealing with such a system theoretically one needs to go beyond the Born–Oppenheimer approximation and solve complex coupled differential equations in order to monitor the nuclear motion simultaneously on more than one electronic state. In such a situation, the adiabatic electronic picture becomes useless as one ends up with diverging kinetic coupling terms

\* Corresponding author. Fax: +49-6221-54-5221.

E-mail addresses: susa@tc.pci.uni-heidelberg.de (S. Mahapatra), horst@tc.pci.uni-heidelberg.de (H. Köppel).

at the point of degeneracy which are difficult to deal with in a numerical treatment. To avoid this difficulty, the complementary diabatic electronic representation [13–15] is preferred in which the diverging kinetic coupling is replaced by a nondiverging potential coupling. Although this concept is well known in the literature, the actual construction of diabatic electronic states for a polyatomic system is still a highly difficult task and has only partly been achieved to date (for a review on this subject, see for example, Ref. [16]).

NO<sub>2</sub> is a well-known triatomic molecule which has an outstandingly complex spectroscopy. Most of the investigations on this system to date are concerned with understanding the highly dense spectral lines in its optical spectra. A review of all the numerous studies is beyond the scope of the present article and, we cite only some key references here, see for example, Refs. [17–34]. Already in mid-1970, the theoretical work of Gillispie et al. [25,26] and Jackels and Davidson [27,28] revealed that the ground electronic state of NO<sub>2</sub> ( $\tilde{X}^2A_1$ ) undergoes a curve crossing with several doublet excited electronic states ( $\tilde{A}^2B_2$ ,  $\tilde{B}^2B_1$  and  $\tilde{C}^2A_2$ ). The ground electronic state is coupled with the  $\tilde{A}^2B_2$  electronic state through the asymmetric stretching vibrational mode at relatively low energy where their PESs form a *conical intersection*. The ground electronic state also becomes degenerate with the  $\tilde{B}^2B_1$  electronic state at the linear geometry and forms there a Renner–Teller pair [35]. The  $\tilde{A}^2B_2$  and  $\tilde{B}^2B_1$  electronic states are optically bright, whereas the  $\tilde{C}^2A_2$  electronic state is optically dark for a transition from the  $\tilde{X}^2A_1$  electronic state. The  $\tilde{C}^2A_2$  state is coupled to the  $\tilde{B}^2B_1$  state via the asymmetric stretching vibrational mode (at much higher energy) and again forms another conical intersection.

The complexity in the visible absorption spectrum of NO<sub>2</sub> (with increasing energy) is known to be caused mainly by the nonadiabatic couplings associated with the conical intersection between the  $\tilde{X}^2A_1$  and  $\tilde{A}^2B_2$  electronic states. Therefore, almost all theoretical studies on the NO<sub>2</sub> absorption spectrum have focussed on the  $\tilde{X}^2A_1/\tilde{A}^2B_2$  coupled electronic manifold. NO<sub>2</sub> is a strongly bent molecule and possesses C<sub>2v</sub> minima [25–28] in both the  $\tilde{X}^2A_1$  and  $\tilde{A}^2B_2$  electronic states. The

barrier to linearity in the  $\tilde{X}^2A_1$  electronic state is  $\sim 1.83$  eV [29,30]. The locus of the degeneracy between the  $\tilde{X}^2A_1$  and  $\tilde{B}^2B_1$  electronic states (Renner–Teller coupling) remains energetically well above the minimum energy of the  $\tilde{A}^2B_2$  state and this coupling is not expected to have any drastic influence on the low-energy vibrational structure of the absorption band.

The equilibrium geometry of NO<sub>2</sub> in its  $\tilde{X}^2A_1$  state occurs at a bond distance  $r \approx 1.20$  Å and a bond angle  $\phi \approx 134^\circ$ , that in the  $\tilde{A}^2B_2$  electronic state at  $r \approx 1.26$  Å and  $\phi \approx 102^\circ$  [25,26]. Therefore, owing to the large change in the equilibrium bond angle of the  $\tilde{X}^2A_1$  and  $\tilde{A}^2B_2$  electronic states, the low-lying vibrational levels of the latter electronic state are difficult to probe in optical spectroscopy. The equilibrium geometry of NO<sub>2</sub><sup>−</sup> occurs at  $r = 1.25 \pm 0.02$  Å and  $\phi = 117.5 \pm 2^\circ$  [31] and is closer to that of the  $\tilde{A}^2B_2$  state of the neutral; therefore, negative ion photoelectron spectroscopy has been successfully utilized by Weaver et al. [32] to observe the transition to the low-lying vibrational levels of the  $\tilde{A}^2B_2$  electronic state of NO<sub>2</sub> by using a 4.66 eV laser beam. The photoelectron spectra of NO<sub>2</sub><sup>−</sup> for a transition to the  $\tilde{X}^2A_1$  state of NO<sub>2</sub> was also recorded by Ervin et al. [31] at high resolution using a 3.532 eV laser beam.

In an earlier study, we have theoretically calculated the photoelectron bands for the  $\tilde{X}^2A_1$  and  $\tilde{A}^2B_2$  states of NO<sub>2</sub> employing a model diabatic Hamiltonian and using ab initio data from the literature [34]. Our results were shown to compare well with the experimental results of Ervin et al. [31] and Weaver et al. [32]. Particularly, we have shown that the nonadiabatic coupling leads to distinct line splittings under each peak of the (regular) experimental envelope of the  $\tilde{A}^2B_2$  photoelectron band. These line splittings are not resolved due to the limited experimental resolution of a photoelectron spectrum. We estimated error bounds of the key quantity in our approach, the so-called linear vibronic coupling constant  $\lambda$ , from different ab initio results and from the requirement that the regular experimental envelope be properly reproduced. This leads to the limits  $0.07 \leq \lambda \leq 0.1$  eV in the vicinity of the minimum of the seam of conical intersections, with an average value of 0.087 eV for this quantity. The presence of these

line splittings is an important signature of the  $\tilde{X}^2A_1$ – $\tilde{A}^2B_2$  conical intersection and bridges the gap between the photoelectron and the low-energy optical absorption spectrum. Since all evidence for these line splittings is theoretical so far, an effort seems appropriate to go beyond the approach of Ref. [34] and further support these predictions.

In this paper, we report new PESs for the  $\tilde{X}^2A_1$ – $\tilde{A}^2B_2$  conically intersecting manifold of  $\text{NO}_2$  using configuration-selecting multi-reference configuration-interaction method [36]. We note that a global adiabatic PES for the  $\tilde{X}^2A_1$  state of  $\text{NO}_2$  has been recently reported by Grebenshchikov et al. [37]. We diabatize our calculated potential energy data with the aid of a conceptually simple but efficient scheme in which the leading derivative coupling terms becomes sufficiently small [38–40]. The features of these new PESs are compared with those available in the literature. The magnitude of  $\lambda$  extracted from the present more elaborate PESs turns out to reproduce our earlier estimate of this quantity. Employing these new *ab initio* data we study the dynamics of  $\text{NO}_2$  by a time-dependent wave packet approach. We calculate the photodetachment spectrum of  $\text{NO}_2^-$  for a transition to the  $\tilde{A}^2B_2$  state of  $\text{NO}_2$ . We also discuss on the time-dependent dynamics driven by the nonadiabatic coupling, namely a femtosecond decay of the  $\tilde{A}^2B_2$  diabatic electronic population and the time evolution of the wave packet. The latter particularly gives useful insight into the internal conversion process. The present results obtained using more general and more accurate PESs show very good agreement with the experimental results of Weaver et al. [32] and thus corroborate our earlier work employing a model diabatic Hamiltonian [34].

The rest of the paper is structured in the following way. In Section 2, we describe the theoretical methodologies for calculating the PESs and the photodetachment spectrum through wave packet propagation. In Section 3, we first discuss on the topology of the PESs and the nonadiabatic couplings between them and then present the photoelectron spectrum of  $\text{NO}_2^-$  and compare it with the experimental results. We also discuss on the decay of diabatic electronic populations and the wave packet “trajectories” in the coupled

electronic manifold. The paper is closed with a succinct summary in Section 4.

## 2. Theoretical methodology

For the quantum dynamical simulations, to be described below, we employ a diabatic electronic representation [13–15]. This avoids the singularities of the adiabatic electronic states at conical intersections [1–4] and is much easier to deal with numerically. Its construction proceeds in two steps. First, the adiabatic energies of the two states are computed on a three-dimensional grid. From this data an analytic representation of a raw potential energy matrix is derived using an auxiliary two-dimensional grid that resolves the behavior near the conical intersection seam in the direction of the asymmetric stretch. Second, diabatic PESs for the wave packet simulations are constructed from this data.

### 2.1. *Ab initio* calculation and representation of the potential energy surfaces

Adiabatic three-dimensional PESs were computed using the configuration-selecting multi-reference configuration-interaction method [36] with the cc-pVTZ basis set [41] in a massively parallel implementation [42,43]. All 17 valence electrons have been correlated, with five orbitals being retained in the active space and five being inactive. This amounts to a total space of 6,309,096 configurations which are singly and doubly excited with respect to the reference space. Out of these, 660,752 configurations have been selected for the ground state, using a threshold of  $10^{-4}$  for their coefficients in the MRD-CI wave function. This leads to a total weight of the reference configurations of 89–92% and a ground state energy (at equilibrium) of  $-204.722439E_h$ . The latter number is included in Table 2 below and further discussed in Section 3.1.

The calculations were carried out in  $C_s$  symmetry using state-averaged approximate natural orbitals generated with MR-BWPT [44,45]. We used an initial grid in  $(r = (r_1 + r_2)/2, \phi, \Delta r = (r_1 - r_2))$ ,  $r = 1.1$ – $1.5$  Å (in steps of 0.05),  $\phi =$

60–180° (in steps of 20°) and  $\Delta r = 0.0, 0.1, 0.2, 0.4$  and  $0.8 \text{ \AA}$ , thus generating 315 data points. This data alone however is insufficient to obtain an accurate representation of the PES near the conical intersection, in particular in the direction of the asymmetric stretch. We therefore determined the location of the conical intersection  $\phi_c(r)$  for each of the radial data points  $r$ . Through each of these points  $(r, \phi_c(r))$ , we then computed a one-dimensional cut through the conical intersection  $V_{\pm}(r, \phi_c(r), \Delta r)$  as a function of  $\Delta r = 0.00, 0.04, 0.08, 0.16, 0.20, 0.40$  and  $0.80 \text{ \AA}$ . From this data, we extracted a two-dimensional polynomial fit (in  $r$  and  $\Delta r$ ) of the gap at the intersection seam

$$D(r, \Delta r) = V_+(r, \phi_c(r), \Delta r) - V_-(r, \phi_c(r), \Delta r). \quad (1)$$

Using this analytic form for  $D$ , we compute quantities  $A(r, \phi, \Delta r)$  and  $B(r, \phi, \Delta r)$  on the three-dimensional grid such that the eigenvalues  $V_{\pm}$  of

$$\begin{pmatrix} A(r, \phi, \Delta r) & D(r, \Delta r) \\ D(r, \Delta r) & B(r, \phi, \Delta r) \end{pmatrix} \quad (2)$$

are equal to the computed energies on all points of the lattice. Once  $D$  is specified, this assignment is unique. To obtain a simple analytical representation of  $D$ , we note that the leading term must be linear in  $\Delta r$  in order that all matrix elements in Eq. (2) are smooth functions of the coordinates [1]. However, since  $D$  does not depend on  $\phi$ , it is thus possible to generate complex numbers for  $A$  and  $B$  far from the conical intersection. In order to avoid this problem, we regularized  $D$  by subtracting a term proportional to  $(\Delta r)^2$ . In conjunction with the primary, leading term in  $D$ , which is linear in  $\Delta r$ , a parabolic dependence in  $\Delta r$  results for every  $r$  value considered. Note that with the inclusion of this term, all energies could be reproduced by the eigenvalues of Eq. (2). For  $C_{2v}$  geometries, i.e.  $\Delta r = 0$  and  $D(r, \Delta r) = 0$ ,  $A$  and  $B$  reduce to the energies of the states. Near the conical intersection, for small values of the asymmetric stretch we obtain

$$V_{\pm}(r, \phi_c(r), 0) \approx V(r, \phi_c(r), 0) \pm |D(r, \phi_c(r), \Delta r)|,$$

where  $V$  is the energy at the conical intersection. As a result of this procedure,  $A$  and  $B$  vary as smooth, analytic functions of all variables even in

regions of the PES where the energies  $V_{\pm}$  contain strong nonanalytic components. It is thus possible to interpolate  $A$ ,  $B$  and  $D$  by three-dimensional spline fits everywhere and to ultimately compute the energies at any point in space by solving for the eigenvalues of Eq. (2) using the interpolations for  $A$ ,  $B$  and  $D$ .

## 2.2. Construction of diabatic electronic states

The above potential energy matrix (2) has been introduced for the sake of allowing for an analytic representation and spline interpolation of the potential matrix elements. We now proceed to the actual construction of (approximate) diabatic electronic states, by a suitable orthogonal transformation of the adiabatic states. While exactly diabatic states do not exist in general, various approximate construction schemes have been proposed in the literature [16]. A particularly simple approach [38–40] is based on the observation that the singularities associated with the adiabatic basis are caused by the leading terms of a Taylor series (in the diabatic basis) around the locus of degeneracy. These leading terms can be determined from the adiabatic PES alone [38–40] and can then be used to construct the aforementioned orthogonal transformation (of the adiabatic electronic states).

In the present work, we give the main ideas and the resulting working equations and refer the reader to the literature for their derivation and further discussion [38–40]. Let  $V_{\pm}$  be the general adiabatic surfaces, constructed according to Section 2.1 and  $V_{1,2}^0 = V_{1,2}(r_1 = r_2)$  their “ $C_{2v}$  part” as obtained for equal bond lengths. (The latter quantities are symmetry-adapted and, thus, do not possess an energetic ordering like their more general counterparts  $V_{\pm}$ .) Then, an important auxiliary potential matrix,  $U^{(1)}$ , can be written as

$$U^{(1)} = \begin{pmatrix} V_1^0 & \lambda_r \Delta r \\ \lambda_r \Delta r & V_2^0 \end{pmatrix} \quad (3)$$

with [1]

$$\lambda_r = \left[ \frac{1}{8} \frac{\partial^2}{\partial (\Delta r)^2} (V_+ - V_-)^2 \right]_{\Delta r=0}^{1/2}. \quad (4)$$

The vibronic coupling constant should be chosen so as to guarantee the correct lifting of the degeneracy along  $\Delta r$  for any point at the seam of degeneracy; i.e., in general it depends on the values of the other coordinates, here  $r$  and  $\phi$ . For the actual determination of  $\lambda_r$  in the present case, see Section 3 below. Given this proper choice of  $\lambda_r$ , the elements of  $\mathbf{U}^{(1)}$  correctly describe the lifting of the degeneracy of  $V_{\pm}$  when moving away from the conical intersection;  $V_1^0 - V_2^0$  accounts for this lifting in the  $C_{2v}$  subspace, while  $\lambda_r \Delta r$  accounts for it when the bond lengths become unequal. It follows that the derivative couplings between eigenvectors of  $\mathbf{U}^{(1)}$  correctly reproduce the singular part of the full derivative couplings under consideration (see the Appendix of Ref. [38]). The eigenvector matrix of  $\mathbf{U}^{(1)}$  thus serves to define the adiabatic-to-diabatic orthogonal transformation matrix because the singular derivative coupling terms are then eliminated exactly. When this transformation is applied to the diagonal matrix of general adiabatic PESs  $V_{\pm}$ , after some algebra one arrives at the full diabatic potential matrix  $\mathbf{U}$  according to Refs. [38–40]:

$$\mathbf{U} = \frac{V_+ + V_-}{2} \mathbf{1} + \frac{(V_+ - V_-)/2}{\sqrt{\lambda_r^2 \Delta r^2 + (\Delta V_0/2)^2}} \begin{pmatrix} \frac{\Delta V_0}{2} & \lambda_r \Delta r \\ \lambda_r \Delta r & -\frac{\Delta V_0}{2} \end{pmatrix}, \quad (5)$$

with  $\Delta V_0 = V_2^0 - V_1^0$ . Eq. (5) represents the diabatic potential matrix which is used in the present work. Its accuracy has been successfully tested for coupled excited states of  $O_3$  and  $H_2S$  [39,40].

### 2.3. Wave packet dynamics and calculation of the photodetachment spectrum

The quantum dynamics in the interacting  $\tilde{X}^2A_1$  and  $\tilde{A}^2B_2$  electronic states of  $NO_2$  is treated by using the diabatic electronic representation introduced above. Thus, the elements of the vibronic Hamiltonian are weakly varying function of the nuclear coordinates and the kinetic energy operator can be taken as diagonal. Similarly, for the matrix elements of the transition operator the Condon approximation can be explicitly utilized.

The vibronic Hamiltonian for the  $\tilde{X}^2A_1/\tilde{A}^2B_2$  electronic manifold of  $NO_2$  is written as

$$\mathcal{H} = \mathcal{H}^{Nu} + \mathcal{H}^{el},$$

$$= T_N \begin{pmatrix} 1 & 0 \\ 0 & 1 \end{pmatrix} + \begin{pmatrix} U_{11} & U_{12} \\ U_{21} & U_{22} \end{pmatrix}, \quad (6)$$

where  $\mathcal{H}^{Nu}$  and  $\mathcal{H}^{el}$  refer to the nuclear and the electronic part of the Hamiltonian matrix,  $T_N$  is the nuclear kinetic energy operator and  $U_{ij}$  represent the elements of the potential matrix  $\mathbf{U}$ , Eq. (5). As mentioned above,  $NO_2$  is a strongly bent molecule and has a  $C_{2v}$  minimum in both the  $\tilde{X}^2A_1$  and  $\tilde{A}^2B_2$  electronic states. Therefore, to exploit this symmetry explicitly in the nuclear dynamics we write down the elements of the above Hamiltonian matrix in terms of symmetry adapted Jacobi coordinates pertinent to the  $C_{2v}$  point group in the body-fixed frame. Since the dissociation channels are not considered in the present dynamical treatment, the use of such Jacobi coordinates simplifies the numerical treatment [46]. In what follows, we refer to  $r_v$  as the distance between the two terminal O atoms,  $r_d$  as the distance between the N atom and the center-of-mass of the two O atoms and  $\gamma$  as the angle between  $\vec{r}_v$  and  $\vec{r}_d$ . In the following, we restrict the treatment to total angular momentum  $J = 0$ . The nuclear kinetic energy operator is then given by

$$T_N = -\frac{\hbar^2}{2\mu} \frac{\partial^2}{\partial r_d^2} - \frac{\hbar^2}{2\mu'} \frac{\partial^2}{\partial r_v^2} - \frac{\hbar^2}{2I} \frac{1}{\sin \gamma} \frac{\partial}{\partial \gamma} \left( \sin \gamma \frac{\partial}{\partial \gamma} \right),$$

$$\mu = \frac{m_O m_N}{m_O + 2m_N},$$

$$\mu' = \frac{m_O}{2},$$

$$\frac{1}{I} = \frac{1}{\mu r_d^2} + \frac{1}{\mu' r_v^2}. \quad (7)$$

The quantities  $m_O$ ,  $m_N$  and  $I$  in the above equation denote the masses of the oxygen and nitrogen atoms and the three-body moment of inertia, respectively.

In the time-dependent picture the golden rule expression for the intensity of the photodetachment spectrum is given by [1]

$$P(E) \approx \text{Re} \int_0^\infty e^{iEt/\hbar} \langle \Psi(0) | e^{-i\mathcal{H}t/\hbar} | \Psi(0) \rangle dt, \quad (8)$$

where

$$|\Psi(0)\rangle = |\Psi(t=0)\rangle = \begin{pmatrix} \tau_1 \\ \tau_2 \end{pmatrix} |\chi\rangle \quad (9)$$

plays the role of the initial wave function of  $\text{NO}_2^-$  prepared on the electronic state of  $\text{NO}_2$  through a Franck–Condon transition. The quantities  $\tau_1$  and  $\tau_2$  are the matrix elements of the transition operator for the two electronic states ( $\tilde{\text{X}}^2\text{A}_1$  and  $\tilde{\text{A}}^2\text{B}_2$ , respectively) and are weakly varying functions of the nuclear coordinates in a diabatic electronic basis.  $|\chi\rangle$  corresponds to the nuclear wave function of  $\text{NO}_2^-$  in its electronic and vibrational ground state which is taken to be the direct product of harmonic oscillator wave functions of the  $\text{NO}_2^-$  ground electronic state.

The action of the exponential operator  $e^{-i\mathcal{H}t/\hbar}$  on the initial wave function  $|\Psi(0)\rangle$  in Eq. (8) is carried out numerically on a grid in  $(r_d, r_v, \gamma)$  space. We construct an equally spaced grid along  $r_d$  and  $r_v$ . The grid points along  $\gamma$  are taken as the nodes of a  $n$ -point Gauss–Legendre quadrature. The total time  $t$  is divided into  $N$  segments of length  $\Delta t$  and the exponential operator at each time step is approximated by the second-order split-operator method [47]. The action of the resulting exponential containing the radial kinetic energy operators is carried out by the fast Fourier transform method [48] and that containing the angular kinetic energy operator by the discrete variable representation method [49–51]. The grid parameters used in calculating the photodetachment spectrum are given in Table 1.

The different spatial symmetries of the interacting electronic states lead to the presence of a vibronic symmetry, i.e. the vibronic secular matrix becomes block-diagonal upon a suitable ordering

of basis states [1]. Consequently, the golden rule expression (Eq. (8)) reduces to

$$P(E) = \sum_{i=1}^2 |\tau_i|^2 \text{Re} \int_0^\infty e^{iEt/\hbar} C_i(t) dt, \quad (10)$$

where  $C_i(t) [= \langle \chi_i(0) | \chi_i(t) \rangle]$  is the time autocorrelation function for the respective diabatic electronic state  $i$ .

### 3. Results and Discussion

#### 3.1. Potential energy surfaces

The potential energy data at the computed ab initio points are obtained from the eigenvalues of Eq. (2) and the additional data in between the computed grid points are generated through the three-dimensional spline interpolation method mentioned above. In Fig. 1(a), the cuts of the PES at the  $\text{C}_{2v}$  geometry of  $\text{NO}_2$  are shown as a contour line diagram in the  $r$ – $\phi$  plane. Remember that, apart from the correlation of electronic states on both sides of the crossing seam, the adiabatic and diabatic representations coincide here. In the figure, we show the diabatic electronic surfaces which are smooth functions of  $r$  and  $\phi$  also at the seam and possess the same symmetry for all  $\text{C}_{2v}$  conformations. The contours for the  $\tilde{\text{X}}^2\text{A}_1$  and  $\tilde{\text{A}}^2\text{B}_2$  electronic states are shown by the dashed and solid curves, respectively. The seam of conical intersections between these two surfaces is shown by the single full line. It can be seen that the intersection seam is essentially independent of the bond angle. The cross on the seam indicates the energetic minimum on this seam. The filled circle in the diagram indicates the location of the

Table 1

Numerical grid parameters used in the wave packet propagation for calculating the photodetachment spectrum

Parameters		
$N_{r_d}/N_{r_v}/N_\gamma$	64/64/49	Number of grid points
$r_{d\min}/r_{d\max}$ ( $a_0$ )	0.05/2.00	Extension of the grid along $r_d$
$r_{v\min}/r_{v\max}$ ( $a_0$ )	2.50/5.50	Extension of the grid along $r_v$
$\Delta t$ (fs)	0.1347	Length of the time step used in the WP propagation
$T$ (ps)	2.204	Total propagation time

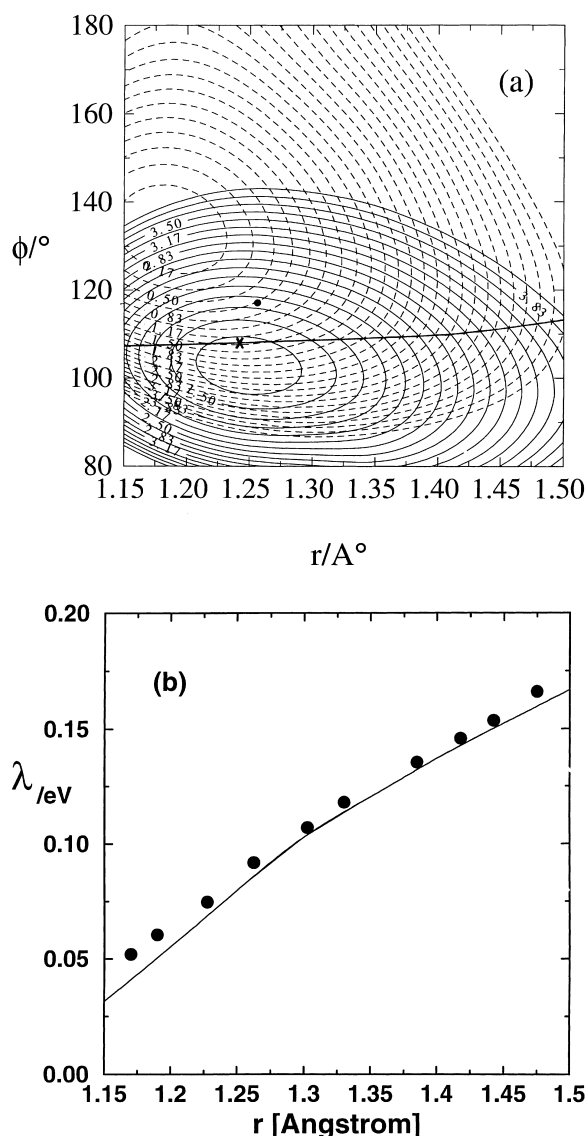


Fig. 1. (a) Contours of the potential energies (eV) of the  $\tilde{X}^2A_1$  (---) and  $\tilde{A}^2B_2$  (—) electronic states plotted in the  $r$ - $\phi$  plane for the  $C_{2v}$  geometry of NO<sub>2</sub>. The full straight line in the figure indicates the seam of conical intersections between these two electronic states. The location of the energetic minimum on this seam is shown by the cross. The full dot denotes the FC zone centre. (b) Variation of the linear vibronic coupling parameter  $\lambda$  with the bond length  $r$ . The solid line indicates the value of  $\lambda$  obtained for a fixed bond angle 108.3° (near the minimum of the seam of intersections) and the filled circles indicate its value calculated along the crossing seam of Fig. 1(a).

Franck–Condon zone center for the photodetachment process. The locations and energies of

various stationary points are given in Table 2 along with their experimental values. The minimum of the  $\tilde{A}^2B_2$  electronic state occurs at 1.207 eV relative to the minimum of the  $\tilde{X}^2A_1$  electronic state. The minimum of the seam of conical intersections (here called cusp) occurs at 1.287 eV relative to the  $\tilde{X}^2A_1$  state minimum. As can be seen from the above estimate, the minimum of the seam of conical intersections is only 0.08 eV above the minimum of the  $\tilde{A}^2B_2$  state, which is less than a quantum of the bending vibration of NO<sub>2</sub> in this state. Since nonadiabatic effects are known to be strong above the minimum energy of the seam, even the low-lying vibrational levels of the  $\tilde{A}^2B_2$  state are expected to be affected by the nonadiabatic coupling [1].

The equilibrium geometries of NO<sub>2</sub> in its various electronic states have been calculated by various authors and each of them reported slightly different values for  $r$  and  $\phi$ . We note only a few of them here. For example, the equilibrium geometry on the ab initio PESs of Hirsch et al. [52] occurs at  $r = 1.203$  Å and  $\phi = 133.6^\circ$  for the  $\tilde{X}^2A_1$  state and at  $r = 1.277$  Å and  $\phi = 101.9^\circ$  for the  $\tilde{A}^2B_2$  state. The above quantities reported by Gillispie et al. [25,26] at  $r = 1.199$  Å,  $\phi = 134.5^\circ$  and  $r = 1.263$  Å,  $\phi = 101.7^\circ$  for the  $\tilde{X}^2A_1$  and  $\tilde{A}^2B_2$  states, respectively. Kaldor [53,54] has given a comprehensive account of the sensitivity of the above parameters on the choice of a particular basis set and the ab initio method of computation. The equilibrium geometry for the  $\tilde{X}^2A_1$  state reported recently by Grebenshchikov et al. [37] occurs at  $r = 1.227$  Å and  $\phi = 137.5^\circ$ . From Table 2, it can be seen that the equilibrium geometries obtained from our three-dimensional PESs compare well with those mentioned above as well as with the experimental values [29–31,55]. The experimental determination of the structural parameters for the  $\tilde{A}^2B_2$  state is cumbersome because the minimum of this state is very near to the  $\tilde{X}^2A_1/\tilde{A}^2B_2$  cusp, and therefore, strongly affected by the nonadiabatic interactions. The energy of the  $\tilde{A}^2B_2$  state minimum is reported as 1.18 eV by Gillispie et al. [25,26] and as 1.06 and 1.08 eV by Blahous et al. [56] and Hirsch et al. [52], respectively (relative to the  $\tilde{X}^2A_1$  state minimum). It can be seen from Table 2 that our result



Table 2

Geometries and energy parameters for the  $\tilde{X}^2A_1$  and  $\tilde{A}^2B_2$  stationary points and the  $\tilde{X}^2A_1/\tilde{A}^2B_2$  cusp of  $NO_2$  obtained from the three-dimensional fit to the present PESs along with their experimental values

	$NO_2$						$NO_2^-$	
	$\tilde{X}^2A_1$		$\tilde{A}^2B_2$		Cusp		Present	Experiment <sup>d</sup>
	Present	Experiment <sup>a</sup>	Present	Experiment <sup>b</sup>	Present	Experiment <sup>c</sup>		
$r$ (Å)	1.186	1.194	1.247	–	1.242	1.246	1.257	$1.25 \pm 0.02$
$\phi$ (deg)	133.6	133.9	102.6	–	108.04	103.1	117.2	$117.5 \pm 2$
$E$ (eV)	0.0 <sup>e</sup>	0.0	1.207	$1.210 \pm 0.012$	1.287	$1.21 \pm 0.09$	–	–

<sup>a</sup> Values from Refs. [29,30,55].

<sup>b</sup> Values from Ref. [63].

<sup>c</sup> Values from Refs. [64–66].

<sup>d</sup> Values from Ref. [31].

<sup>e</sup> Absolute value  $-204.722439E_h$ .

of 1.207 eV for this quantity is closer to its experimental value. The recent results of Grebenshchikov et al. [37] indicated an energy difference of  $\sim 1.21$  eV between the two stationary points of the ground state adiabatic PES. Krebs and Buenker [57] obtained a value of 1.265 eV for the  $\tilde{A}^2B_2$  minimum relative to that of the  $\tilde{X}^2A_1$  using a full configuration-interaction algorithm. The  $\tilde{X}^2A_1/\tilde{A}^2B_2$  cusp is reported at  $r = 1.259$  Å and  $\phi = 107.4^\circ$  by Hirsch et al. [52] and at  $r = 1.26$  Å,  $\phi = 114^\circ$  and  $r = 1.267$  Å,  $\phi = 107.8^\circ$  by Gillispie et al. [25,26] and by Hirsch and Buenker [58], respectively. The energy at the cusp is reported at 1.14, 1.48 and 0.96 eV relative to the  $\tilde{X}^2A_1$  state minimum by the above three authors, respectively, in that order. It can be seen from Table 2 that the value of  $r$  obtained by us at the cusp falls slightly below the values noted above; however, it is closer to the corresponding experimental value. The energy at the cusp obtained by us also compares well with that of the experimental one within the error bars. Finally, an absolute energy at the  $\tilde{X}^2A_1$  state minimum of  $-204.722439E_h$  is also reported and may be compared with earlier literature data of Hirsch and Buenker ( $-204.4118E_h$ ) [58] and the extrapolated values of Krebs and Buenker [ $E$  (zero threshold) =  $-204.67977137E_h$  and  $E$  (full-CI) =  $-204.73495163E_h$ ] [57]. We note that our number represents the calculated value of this minimum without any extrapolation, and still, is only slightly higher than the full-CI estimate of Krebs and Buenker [57]. This gives evidence for the high

quality of our electronic structure calculations. For a collection of other theoretical data on the stationary points of the  $\tilde{X}^2A_1/\tilde{A}^2B_2$  electronic states of  $NO_2$ , we refer the reader to the tables given in Refs. [25,26,52–54,57].

In order to arrive at the diabatic potential matrix, (Eq. (5)) we now determine  $\lambda_r$  according to Eq. (4) using finite differences. The derivative should be taken for  $r$  and  $\phi$  values along the seam of intersections (full line in Fig. 1(a)). Since this seam is close to a horizontal straight line in the figure, we may also compare this with a simplified treatment where  $\phi$  is fixed at a suitable average value along the seam. Furthermore, we convert  $\lambda_r$  to a “normal coordinate representation” according to

$$\lambda_r \Delta r = \lambda Q_u, \quad (11)$$

where  $Q_u$  is the dimensionless normal coordinate of the asymmetric stretching mode. Since  $Q_u = 6.16 \Delta r/a_0$ , this amounts only to a change of scale which, however, facilitates comparison with previous work. The resulting  $\lambda$  is plotted as function of the bond length  $r$  for a fixed value of the bond angle  $108.33^\circ$  (near the minimum of the seam of intersections) in Fig. 1(b). The values of  $\lambda$  obtained along the seam are included in the panel by filled circles. Here, the value of  $\phi$  is always between  $108^\circ$  and  $113^\circ$  (see the full line in Fig. 1(a)) and, correspondingly, the two sets of  $\lambda$  values are very close to each other. It can be seen that  $\lambda$  grows almost linearly with  $r$ . The region of the space

which is relevant for the photodetachment spectrum is well covered by  $r < 1.35$  Å and the magnitude of  $\lambda$  lies within 0.1 eV in that region. This confirms our earlier estimate of  $\langle \lambda \rangle = 0.087$  eV in the vicinity of the minimum of the seam of conical intersections that was used to simulate the photodetachment spectrum using a model diabatic Hamiltonian [34].

We note that a small value of  $\lambda \sim 0.035$  eV has also been reported by Delon and Jost [20]. They obtained this value by analyzing their laser induced fluorescence spectral data. We also extracted  $\lambda$  in the vicinity of the minimum of the seam of intersections from the earlier work of Hirsch and Buenker [58], as well as from the recent work of Hirsch et al. [52,59]. From the earlier work of Hirsch and Buenker [58], we obtain  $\lambda \approx 0.07$  eV which is similar to ours, but the recent work of Hirsch et al. [52,59] revealed  $\lambda \geq 0.3$  eV. The reason of this large difference is not clear at this point. Note, however that the present comparison holds only for the leading terms (in  $\Delta r$ ) of the vibronic coupling element. While in Refs. [20,34] a strictly linear form was assumed, Refs. [52,59] and the present work contain higher order terms (of different functional form) which are not compared here.

The PESs for the  $\tilde{X}^2A_1$  and  $\tilde{A}^2B_2$  states are plotted as contour line diagrams for the  $C_s$  geometry ( $\Delta r = 0.2$  Å) of  $NO_2$  in Fig. 2. The adiabatic potential energies for the  $\tilde{X}^2A_1$  and  $\tilde{A}^2B_2$  states are obtained by diagonalizing the potential energy matrix in Eq. (2) and are shown in Fig. 2(a) by the dashed and solid lines, respectively. The avoided crossings between the two adiabatic PESs along the intersection seam are visible from the figure. Also, the minimum of the upper adiabatic surface occurs at the minimum of this intersection seam. The diabatic PESs obtained by transforming the above adiabatic potential energies using the ansatz illustrated in Section 2.2 are shown as contour line diagrams in Fig. 2(b). The dashed and the solid lines represent the potential energies of the  $\tilde{X}^2A_1$  and the  $\tilde{A}^2B_2$  states, respectively. It can be seen from the figure that the avoided crossings between the adiabatic PESs change to crossings in the diabatic representation and the minimum of the upper diabatic surface shifts to smaller bond angle and larger bond distance compared to the

adiabatic minimum. A very smooth behavior of the diabatic PESs is also apparent from the figure. The coupling elements between the above two diabatic surfaces are shown as a contour line diagram in the  $r$ – $\phi$  plane in Fig. 2(c). The ridge on each contour line occurs at the seam of the conical intersections between the two surfaces. The smooth behavior of the coupling elements in the vicinity of the intersection seam is revealed by the figure. It can also be seen that the coupling between the two surfaces becomes stronger with increasing  $r$ . This agrees with Fig. 1(b) and causes the large increase in the line density with increasing energy in the optical spectrum of  $NO_2$ .

### 3.2. Photodetachment spectrum

In this section, we report on the  $\tilde{A}^2B_2$  photoelectron band of  $NO_2$  and compare it with the experimental recording of Weaver et al. [32]. The 266 nm (4.660 eV) photodetachment spectrum of  $NO_2^-$  measured by Weaver et al. [32] indicated two full bands corresponding to  $\tilde{X}^2A_1$  and  $\tilde{A}^2B_2$  state and the beginning of a third, the dark  $\tilde{C}^2A_2$  state of  $NO_2$ . In our study, we consider only the  $\tilde{X}^2A_1/\tilde{A}^2B_2$  conically intersecting manifold of  $NO_2$ . The photoelectron band for the  $\tilde{X}^2A_1$  state is unaffected by the nonadiabatic coupling [34]. This feature has been reproduced with the present calculations and for brevity, we do not show it here. The main focus of the present work is to accurately treat the nonadiabatic coupling effects and hence to confirm our earlier results based on a model Hamiltonian approach.

The photodetachment spectrum is computed by Eq. (10), i.e. Fourier transforming the time autocorrelation function for the initial wave function  $|\Psi(0)\rangle$  of Eq. (9). The wave function is initially prepared on the  $\tilde{A}^2B_2$  electronic state ( $\tau_1 = 0$ ,  $\tau_2 = 1$ ) of  $NO_2$ . Since we start with a real initial wave function, we apply the prescription of computing  $C(2t) = \langle \Psi^*(t) | \Psi(t) \rangle$ , from the wave function at time  $t$  [60,61]. This prescription allows to increase the energy resolution ( $\Delta E = 2\pi\hbar/T$ ) in the photoelectron spectrum by a factor of two by effectively doubling the total propagation time  $T$ . The photoelectron spectrum obtained by Fourier transforming  $C(2t)$  for the uncoupled (diabatic)

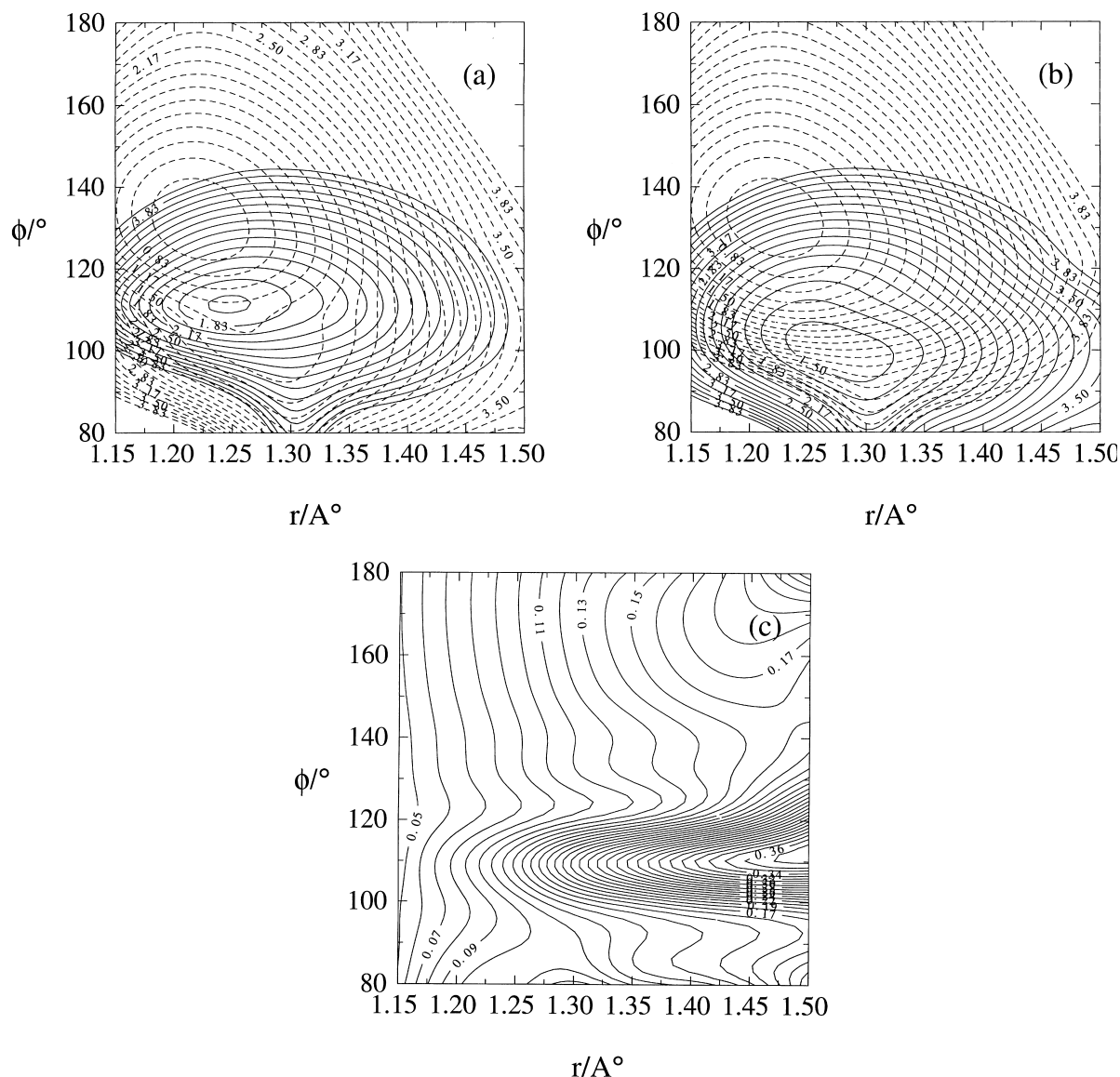


Fig. 2. (a) Contours of the adiabatic potential energies of the  $\tilde{X}^2A_1$  (---) and  $\tilde{A}^2B_2$  (—) electronic states plotted in the  $r$ – $\phi$  plane for the  $C_s$  geometry of  $\text{NO}_2$  (for  $\Delta r = 0.2$  Å) obtained by interpolating the computed ab initio points. (b) The corresponding diabatic potential energy contours obtained by employing the scheme illustrated in Section 2.2. (c) The off-diagonal coupling elements between the above diabatic PESs.

$\tilde{A}^2B_2$  electronic state of  $\text{NO}_2$  is shown in Fig. 3(a). The intensity of the ejected electron (in arbitrary units) is plotted as a function of the internal energy of the final vibronic state ( $E$ ). The latter is related to the kinetic energy of the outgoing electron ( $E_k$ ) by,  $E_k = h\nu - \text{EA} - E$ , with  $h\nu$  being the energy of

the laser photon and EA, the vertical electron affinity of  $\text{NO}_2$ . The energy resolution in the spectrum in Fig. 3(a) is  $\Delta E = 9.36 \times 10^{-4}$  eV. The peaks in the spectrum are  $\sim 0.1$  eV apart in energy and reveal a progression along the bending mode of  $\text{NO}_2$ . The frequency of the symmetric stretch

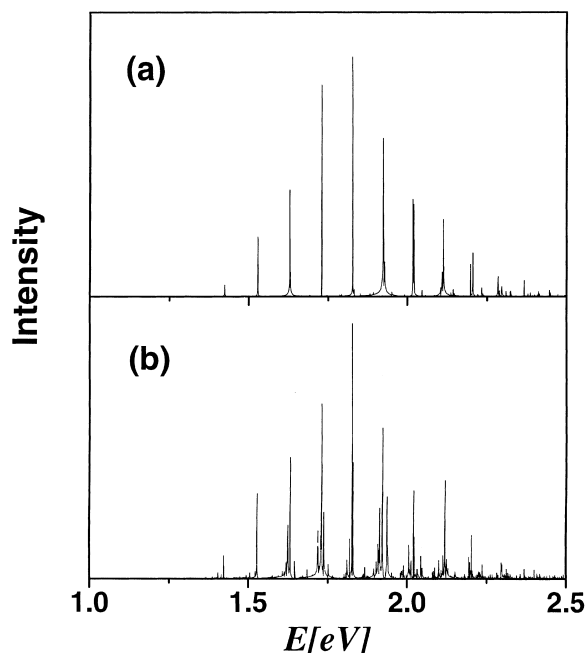


Fig. 3. The photoelectron spectrum of  $\text{NO}_2^-$  for a transition to the  $\tilde{\text{A}}^2\text{B}_2$  state of  $\text{NO}_2$  calculated (a) without and (b) with coupling to the  $\tilde{\text{X}}^2\text{A}_1$  state. The intensity of the photoelectron (in arbitrary units) is plotted as a function of the energy of the final vibronic state. The zero of the energy scale corresponds to the minimum of the  $\tilde{\text{X}}^2\text{A}_1$  electronic state.

vibration is approximately twice that of the bend and the asymmetric stretch vibration has much higher frequency [25,26,34,53,54]. In Fig. 3(a), we do not see any noticeable excitation of the symmetric stretching mode of  $\text{NO}_2$ , and due to symmetry reasons, the asymmetric stretching mode hardly contributes to the spectral progression. Since the extra electron in  $\text{NO}_2^-$  occupies an antibonding molecular orbital, removal of this electron increases the bond angle and decreases the bond length in the neutral. Therefore, an extended progression along the bending mode results on photodetachment. The above spectrum corresponds to the one with  $\lambda = 0.0$  shown in our earlier paper [Fig. 4(a) of Ref. [34]]. It can be seen that the overall structure of the spectrum in Fig. 3(a) agrees nicely with the earlier one.

When including the coupling with the  $\tilde{\text{X}}^2\text{A}_1$  state, we obtain the  $\tilde{\text{A}}^2\text{B}_2$  photoelectron band shown in Fig. 3(b). The energy resolution in this

spectrum is the same as before. The spectrum reveals again a dominant progression of ‘peaks’ ( $\sim 0.1\text{eV}$  spacings) along the bending vibrational mode of  $\text{NO}_2$ . However, most ‘peaks’ in this progression consist of a group of closely spaced lines, where the line splittings are rather small so that a clustering of lines occurs. These line splittings are an effect of the nonadiabatic coupling. The high-energy vibrational levels of the  $\tilde{\text{X}}^2\text{A}_1$  state are mixed with the vibrational levels of the  $\tilde{\text{A}}^2\text{B}_2$  state and the resulting spectral lines are clumped into groups of nonoverlapping ‘resonances’. The additional very minor oscillations near each peak are perhaps arising due to the finite time propagation of the wave packet. It can be seen from Fig. 3(b) that the clustering of lines increases with increasing energy because the nonadiabatic coupling becomes stronger at high energies (Fig. 2(c)) and the density of coupled vibrational states (of upper and lower surfaces) increases. At this point, a remark must be added on the accuracy of the results at high energies. The present PESs are tested to be very accurate (energies are reproduced to within  $0.5\text{ mE}_\text{h}$  across the entire surface) until 2 eV above the global minimum and we rely on extrapolation techniques beyond this energy. Therefore, a slight change in the peak structure beyond 2 eV may result when ab initio points become available at higher energies.

The experimental  $\tilde{\text{A}}^2\text{B}_2$  photoelectron band of Weaver et al. [32] is not resolved enough to discern the above vibronic fine structure. The instrumental resolution is 8 meV at 0.65 eV electron kinetic energy, and degrades as  $E_\text{k}^{3/2}$  at higher electron kinetic energy. In our previous work, we convoluted our high resolution stick spectrum by a Lorentzian function with an energy dependent width of 8 meV HWHM plus an additional 6 meV to account for the rotational broadening in the experimental spectrum [34]. In the time-dependent picture, the above convolution can be achieved by damping the time autocorrelation function by a suitable time-dependent function. We choose to damp the autocorrelation function with an exponential function

$$f(t) = \exp\left(-\frac{t}{\tau_\text{r}}\right), \quad (12)$$

before Fourier transformation. This is the same as convoluting the spectrum in Fig. 3(b) with a Lorentzian function with FWHM  $\Gamma = 2\hbar/\tau_r$ ,  $\tau_r$  being the relaxation time. The spectrum obtained by damping the time autocorrelation function of the energy spectrum in Fig. 3(b) with  $\tau_r = 66$  fs (which corresponds to  $\Gamma = 20$  meV) is presented in the lower panel of Fig. 4. The experimental spectrum of Weaver et al. is included in the upper panel of Fig. 4. It can be seen that the theoretical spectrum compares very well with the experimental one. As expected, it consists basically of a regular progression of the bending mode. Also, the envelope

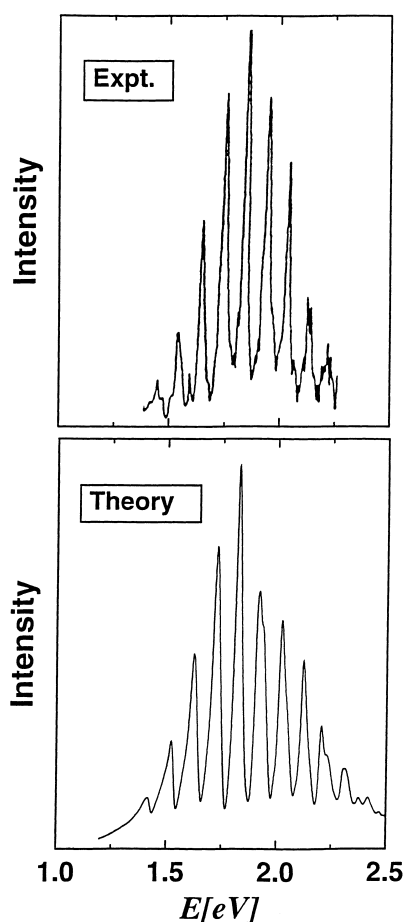


Fig. 4. Same as given in Fig. 3(b), but convoluted by a 20 meV FWHM Lorentzian function (lower panel). The 266 nm (4.66 eV) experimental spectrum of Weaver et al. is reproduced from Ref. [32] and shown in the upper panel.

is quite similar to that we reported earlier with a model Hamiltonian with harmonic diabatic surfaces and with  $\lambda = 0.087$  eV (cf. Fig. 4(b) of Ref. [34]). Most important, is however, that we also clearly reproduce the line splittings which occur under each peak of the low-resolution envelope (cf. Fig. 4(b) of Ref. [34]) with the present Fig. 3(b). This confirms the formation of nonoverlapping resonances as the main effect of the non-adiabatic interaction in this transition. Clearly, suitable experimental studies to verify this prediction would be highly desirable.

### 3.3. Time-dependent dynamics

We now discuss the femtosecond internal conversion dynamics of NO<sub>2</sub> driven by the nonadiabatic interactions. The relevant quantity reported in Fig. 5 is the decay of the  $\tilde{A}^2B_2$  diabatic electronic population in time. The initial wave packet is the same as the one used above to calculate the  $\tilde{A}^2B_2$  photoelectron band (presented in Fig. 3(b)). It can be seen from Fig. 5 that the population of the  $\tilde{A}^2B_2$  state, starting from 1.0 at  $t = 0$ , decays to  $\sim 0.4$  at longer time. In  $\sim 90$  fs, 50% of the population is transferred to the  $\tilde{X}^2A_1$  state. The initial fast decay of the population relates to a decay rate of about 120 fs, which can be obtained by fitting the initial decay curve to an exponential. Therefore, most of the nonradiative or internal conversion processes take place within that time.

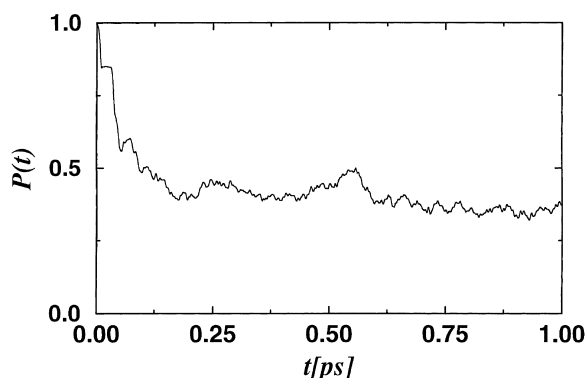


Fig. 5. Decay of the  $\tilde{A}^2B_2$  diabatic population in time. The initial wave packet corresponds to the one used to calculate the spectrum shown in Fig. 3(b).

At longer time, very little population exchange occurs between the  $\tilde{X}^2A_1$  and  $\tilde{A}^2B_2$  electronic states and the  $\tilde{A}^2B_2$  state population more or less fluctuates around the average value of  $\sim 40\%$ . This much of the population therefore remains trapped in the  $\tilde{A}^2B_2$  electronic state. We emphasize that the wiggles in the figure are not a numerical artefact but have been reproduced by varying the grid size. On the other hand, they disappear when increasing the vibronic coupling strength. Similar effects have been found previously in other weakly coupled systems [62] although a precise explanation for the time scale of the oscillations cannot be given at present.

In order to understand the above population dynamics more clearly we show snapshots of the wave packet evolving on the coupled  $\tilde{X}^2A_1/\tilde{A}^2B_2$  electronic manifold at different times in Fig. 6(a)–(f). The probability density of the wave packet averaged over the angular coordinate is superimposed on the potential energy contours for  $\gamma = \pi/2$  in the  $r_d$ – $r_v$  plane. The potential energy contours

indicated by the dashed and solid lines represent the  $\tilde{X}^2A_1$  and  $\tilde{A}^2B_2$  electronic states, respectively. The maximum energy of the potential contour lines in Fig. 6 is 3.5 eV for both states. The seam of conical intersections is indicated by the full line in Fig. 6(a). It can be seen that the initial wave packet is generated directly on this seam. In about 11 fs (panel (b)), the wave packet moves to the minimum of the  $\tilde{A}^2B_2$  state. Afterwards, the larger part continues to move in the same direction on the upper surface, but a smaller part gets “reflected” on the  $\tilde{X}^2A_1$  surface (17.5 fs, panel (c)). After 23 fs (cf. panel (d)) also the part on the upper surface has reached the outer turning point. Both of these times correspond to the early plateau in Fig. 5, where  $\sim 15\%$  of the wave packet have interconverted to the  $\tilde{X}^2A_1$  surface. The next drop in  $\tilde{A}^2B_2$  population occurs at about 50 fs which approximately corresponds to the bending vibrational period in the  $\tilde{A}^2B_2$  electronic state. Within this time  $\sim 40\%$  of the population moves to the  $\tilde{X}^2A_1$  state. Fig. 6(e) approximately corresponds to the time when both

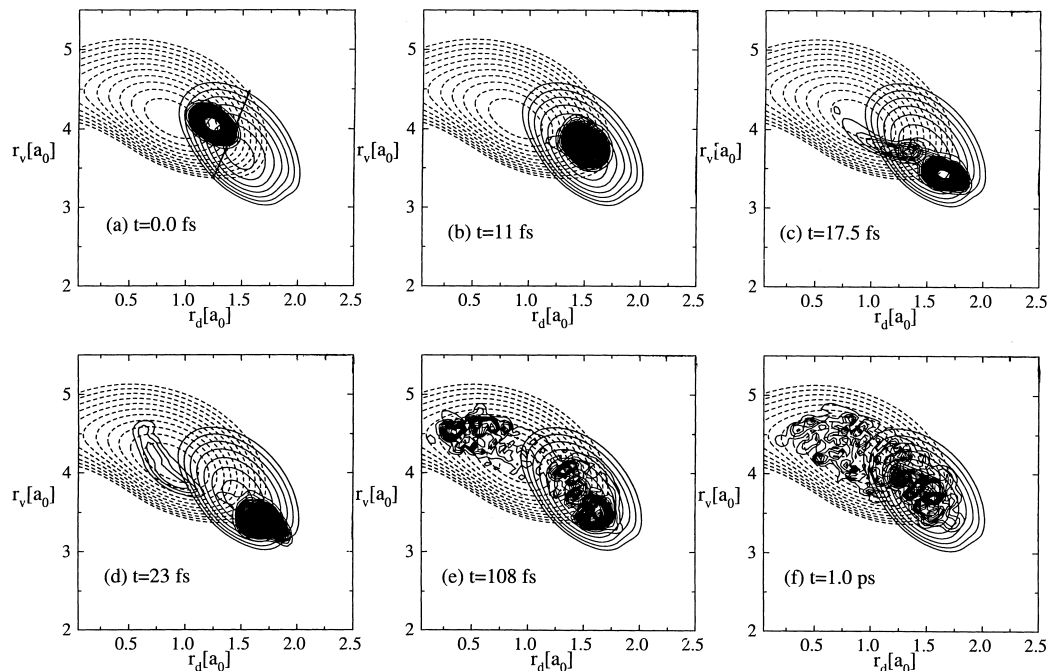


Fig. 6. Probability density ( $|\Psi|^2$ ) of the wave packet averaged over the Jacobi angle and superimposed on the potential energy contours in the  $r_d$ – $r_v$  Jacobi plane for  $\gamma = \pi/2$ . The different times are indicated in each panel. The dashed and solid potential energy contours refer to the  $\tilde{X}^2A_1$  and  $\tilde{A}^2B_2$  electronic states, respectively.

states acquire a 50% population ( $t = 108$  fs). The wave packet in the  $\tilde{A}^2B_2$  state still exhibits a coherent motion, whereas that in the  $\tilde{X}^2A_1$  state looks rather irregular. With increasing time, the wave packet motion becomes irregular also in the  $\tilde{A}^2B_2$  state, as can be seen from the panel (f) for  $t = 1.0$  ps. Correspondingly, also the electronic populations according to Fig. 5 exhibit fluctuating rather than oscillatory behavior.

#### 4. Summary and conclusions

We have presented a combined electronic structure and time-dependent dynamical study on the coupled  $\tilde{X}^2A_1$  and  $\tilde{A}^2B_2$  electronic states of  $\text{NO}_2$ . The PESs are calculated by the configuration-selecting multi-reference configuration interaction method employing the cc-pVTZ basis set. The adiabatic potential energy data are diabaticized utilizing a conceptually simple and efficient scheme, in which the leading derivative coupling terms have been shown to be very small [38]. The stationary points on these new PESs are found to be in good agreement with those from other theoretical studies as well as with the experimental results (Table 2). The  $\tilde{A}^2B_2$  state minimum is found to occur at 1.207 eV above that of the  $\tilde{X}^2A_1$  state minimum. The minimum of the seam of conical intersections (cusp) occurs at 1.287 eV relative to the  $\tilde{X}^2A_1$  state minimum. Using the above potential energy data we have calculated the linear vibronic coupling parameter  $\lambda$  and shown its variation along the seam of conical intersections. We find  $\lambda \leq 0.1$  eV until  $r = 1.35$  Å, corroborating our earlier estimate of this quantity in a model study.

Employing the above coupled  $\tilde{X}^2A_1/\tilde{A}^2B_2$  diabatic PESs we calculate the photodetachment spectrum of  $\text{NO}_2^-$  for a transition to the  $\tilde{A}^2B_2$  electronic state of  $\text{NO}_2$  with the aid of a time-dependent wave packet propagation scheme. The photoelectron band obtained for the  $\tilde{X}^2A_1$  state reveals a similar structure to that we obtained earlier with a model diabatic Hamiltonian. The  $\tilde{A}^2B_2$  photoelectron spectrum originates right at the onset of the nonadiabatic regime (the  $\tilde{X}^2A_1/\tilde{A}^2B_2$  cusp occurs  $\sim 0.08$  eV above the minimum of

the  $\tilde{A}^2B_2$  electronic state). The photoelectron spectrum obtained for the uncoupled  $\tilde{A}^2B_2$  electronic state reveals a progression along the bending vibrational mode of  $\text{NO}_2$ ; the peaks are  $\sim 0.1$  eV apart, which is about a quantum of bending vibration of  $\text{NO}_2$  in the  $\tilde{A}^2B_2$  state. The above uncoupled state spectrum compares well with that we reported earlier for  $\lambda = 0.0$ . The  $\tilde{A}^2B_2$  photoelectron spectrum including the coupling to the  $\tilde{X}^2A_1$  state reveals a main progression of groups of lines along the bending vibrational mode of  $\text{NO}_2$ . The line splittings within each group are an effect of the nonadiabatic interactions in this photoelectron band. Due to these interactions, the high energy vibrational levels of the  $A_1$  state mix with the low-lying vibrational levels of the  $B_2$  electronic state, and the resulting spectral lines are clumped into groups of nonoverlapping ‘resonances’. In this sense, this spectral envelope represents a weakly (to moderately) coupled system. To compare this coupled state spectrum with the experimental recording of Weaver et al. [32], we convoluted it by a Lorentzian function with FWHM of 20 meV. The resulting convoluted spectrum compares well with the experimental one.

A time-domain investigation of the decay of the  $\tilde{A}^2B_2$  diabatic electronic population revealed that the nonradiative internal conversion process to the  $\tilde{X}^2A_1$  electronic state takes place within  $\sim 120$  fs. The population dynamics is further illustrated by investigating wave packet snapshots on the coupled  $\tilde{X}^2A_1/\tilde{A}^2B_2$  electronic manifold at different times. At longer time, both parts of the wave packet, residing on either electronic state, exhibit an irregular behavior and  $\sim 40\%$  of the wave packet remains trapped in the  $\tilde{A}^2B_2$  electronic state.

In conclusion, we have reported highly accurate PESs for the  $\tilde{X}^2A_1$  and  $\tilde{A}^2B_2$  electronic states of  $\text{NO}_2$ . In fact, for the energy range considered (until 2 eV above the global minimum) the present surfaces are believed to be the most accurate ones available in the literature. The results of our earlier study [34] employing a model diabatic Hamiltonian and ab initio data from the literature are all confirmed. This holds, in particular, for the prediction that under each peak of the experimental  $\tilde{A}^2B_2$  photoelectron band [32], there is substantial

vibronic fine structure caused by the nonadiabatic interaction. An experimental verification of this effect would certainly be highly desirable. Theoretically, the present work is also of interest within the context of the diabatization scheme [38–40] adopted. Although for a small system like NO<sub>2</sub> other methods are also feasible, the present successful application should provide a further basis for its use in larger molecules.

### Acknowledgements

S.M. gratefully acknowledges the Alexander von Humboldt Foundation for financial support at an early stage of this project. S.M. is also grateful to R. Schork for his help on the spline interpolation and to J. Gronki for useful discussions on the diabatization scheme. The work at Heidelberg is financially supported in part by the Deutsche Forschungsgemeinschaft. P.S. and W.W. thank the German National Science Foundation for financial support. The electronic structure calculations were carried out on the 256-node CRAY-T3E of the von-Neumann Institute for Computing. Basis sets were obtained from the Extensible Computational Chemistry Basis Set Database of the Pacific Northwest Laboratory.

### References

- [1] H. Köppel, W. Domcke, L.S. Cederbaum, *Adv. Chem. Phys.* 57 (1984) 59.
- [2] R.L. Whetten, G.S. Ezra, E.R. Grant, *Annu. Rev. Phys. Chem.* 36 (1985) 277.
- [3] I.B. Bersuker, V.Z. Polinger, *Vibronic Interactions in Molecules and Crystals*, Springer, Berlin, 1989.
- [4] W. Domcke, G. Stock, *Adv. Chem. Phys.* 100 (1997) 1.
- [5] E. Teller, *J. Phys. Chem.* 41 (1937) 109.
- [6] G. Herzberg, H.C. Longuet-Higgins, *Discuss. Faraday Soc.* 35 (1963) 77.
- [7] T. Carrington, *Discuss. Faraday Soc.* 53 (1972) 27.
- [8] T. Carrington, *Acc. Chem. Res.* 7 (1974) 20.
- [9] E.R. Davidson, *J. Am. Chem. Soc.* 99 (1977) 397.
- [10] D.R. Yarkony, *Rev. Mod. Phys.* 68 (1996) 985.
- [11] D.R. Yarkony, *Acc. Chem. Res.* 31 (1998) 511.
- [12] F. Bernardi, M. Olivucci, M. Robb, *Chem. Soc. Rev.* 25 (1996) 321.
- [13] W. Lichten, *Phys. Rev.* 164 (1967) 131.
- [14] F.T. Smith, *Phys. Rev.* 179 (1969) 111.
- [15] T.F. O'Malley, *Adv. Atom. Mol. Phys.* 7 (1971) 223.
- [16] T. Pacher, L.S. Cederbaum, H. Köppel, *Adv. Chem. Phys.* 84 (1993) 293.
- [17] R.E. Smalley, L. Wharton, D.H. Levy, *J. Chem. Phys.* 63 (1975) 4977.
- [18] D.K. Hsu, D.L. Monts, R.N. Zare, *Spectral Atlas of NO<sub>2</sub> 5530 to 6480 Å*, Academic Press, New York, 1978 and references therein.
- [19] E. Haller, H. Köppel, L.S. Cederbaum, *J. Mol. Spectrosc.* 111 (1985) 377.
- [20] A. Delon, R. Jost, *J. Chem. Phys.* 95 (1991) 5686.
- [21] A. Delon, R. Georges, B. Kirmse, R. Jost, *Discuss. Faraday Soc.* 102 (1995) 117.
- [22] B. Kirmse, A. Delon, R. Jost, *J. Chem. Phys.* 108 (1998) 6638.
- [23] A. Delon, R. Jost, *J. Chem. Phys.* 110 (1999) 4300.
- [24] F. Leonardi, C. Petrongolo, *J. Chem. Phys.* 106 (1997) 10066 and references therein.
- [25] G.D. Gillispie, A.U. Khan, A.C. Wahl, R.P. Hosteny, M. Krauss, *J. Chem. Phys.* 63 (1975) 3425.
- [26] G.D. Gillispie, A.U. Khan, *J. Chem. Phys.* 65 (1976) 1624.
- [27] C.F. Jackels, E.R. Davidson, *J. Chem. Phys.* 64 (1976) 2908.
- [28] C.F. Jackels, E.R. Davidson, *J. Chem. Phys.* 65 (1976) 2941.
- [29] J.L. Hardwick, J.C.D. Brand, *Chem. Phys. Lett.* 21 (1973) 458.
- [30] J.L. Hardwick, J.C.D. Brand, *Can J. Phys.* 54 (1976) 80.
- [31] K.M. Ervin, J. Ho, W.C. Lineberger, *J. Phys. Chem.* 92 (1988) 5405.
- [32] A. Weaver, R.B. Metz, S.E. Bradforth, D.M. Neumark, *J. Chem. Phys.* 90 (1989) 2070.
- [33] Th. Zimmermann, H. Köppel, L.S. Cederbaum, G. Persch, W. Demtröder, *Phys. Rev. Lett.* 61 (1988) 3.
- [34] S. Mahapatra, H. Köppel, L.S. Cederbaum, *J. Chem. Phys.* 110 (1999) 5691.
- [35] Ch. Jungen, A.J. Merer, in: K. Narahari Rao (Ed.), *Molecular Spectroscopy: Modern Research*, vol. 2, Academic press, New York, 1976, p. 127.
- [36] R.J. Bunker, S.D. Peyerimhoff, *Theor. Chim. Acta* 35 (1974) 33.
- [37] S. Yu. Grebenshchikov, C. Beck, H. Flöthman, R. Schinke, S. Kato, *J. Chem. Phys.* 111 (1999) 619.
- [38] A. Thiel, H. Köppel, *J. Chem. Phys.* 110 (1999) 9371.
- [39] J. Gronki, *Diploma Thesis*, University of Heidelberg, 1999.
- [40] J. Gronki, S. Mahapatra, H. Köppel, *J. Chem. Phys.*, submitted for publication.
- [41] T.H. Dunning, *J. Chem. Phys.* 90 (1989) 1007.
- [42] P. Stampfuß, H. Keiter, W. Wenzel, *J. Comput. Chem.* 20 (1999) 1559.
- [43] P. Stampfuß, W. Wenzel, *J. Mol. Struct.: Invited and Contributed Talks of the 1999 WATOC Conference*, in press.
- [44] W. Wenzel, M.M. Steiner, J.W. Wilkins, K.G. Wilson, *Int. J. Quant. Chem.* S30 (1996) 1325.
- [45] W. Wenzel, M.M. Steiner, *J. Chem. Phys.* 108 (1998) 4714.
- [46] H. Müller, H. Köppel, L.S. Cederbaum, *J. Chem. Phys.* 101 (1994) 10263.



- [47] M.D. Feit, J.A. Fleck Jr., A. Steiger, *J. Comput. Phys.* 47 (1982) 412.
- [48] D. Kosloff, R. Kosloff, *J. Comput. Phys.* 52 (1983) 35.
- [49] Z. Bačić, J.C. Light, *Ann. Rev. Phys. Chem.* 40 (1989) 469.
- [50] F. Quéré, C. Leforestier, *J. Chem. Phys.* 92 (1990) 247.
- [51] G.C. Corey, D. Lemoine, *J. Chem. Phys.* 97 (1992) 4115.
- [52] G. Hirsch, R.J. Buenker, C. Petrongolo, *Mol. Phys.* 73 (1991) 1085.
- [53] U. Kaldor, *Chem. Phys. Lett.* 170 (1990) 17.
- [54] U. Kaldor, *Chem. Phys. Lett.* 185 (1991) 131.
- [55] Y. Morino, M. Tanimoto, S. Saito, E. Hirota, R. Awata, T. Tanaka, *J. Mol. Spectromet.* 98 (1983) 331.
- [56] C.P. Blahous, B.F. Yates, Y. Xie, H.F. Schaefer, *J. Chem. Phys.* 93 (1990) 8105.
- [57] S. Krebs, R.J. Buenker, *J. Chem. Phys.* 103 (1995) 5613.
- [58] G. Hirsch, R.J. Buenker, *Can J. Chem.* 63 (1985) 1542.
- [59] E. Leonardi, C. Petrongolo, G. Hirsch, R.J. Buenker, *J. Chem. Phys.* 105 (1996) 9051.
- [60] U. Manthe, H.-D. Meyer, L.S. Cederbaum, *J. Chem. Phys.* 97 (1992) 9062.
- [61] V. Engel, *Chem. Phys. Lett.* 189 (1992) 76.
- [62] U. Manthe, H. Köppel, *J. Chem. Phys.* 93 (1990) 1658.
- [63] E.R. Davidson, *Int. J. Quant. Chem.* 8 (1974) 83.
- [64] J.C.D. Brand, K.J. Cross, A.R. Hoy, *Can J. Phys.* 57 (1979) 428.
- [65] A.J. Merer, K.-E.J. Hallin, *Can J. Phys.* 56 (1978) 838.
- [66] M. Krauss, R.J. Cellota, S.R. Mielczarek, C.E. Kuyatt, *Chem. Phys. Lett.* 27 (1974) 285.